

## Supplementary information

### *Electron microscopy*

Human mitoribosomes were prepared as previously described (2). Aliquots of 3  $\mu$ l of purified mitoribosomes at a concentration of  $\sim$ 80 nM (0.23 mg/ml) were incubated for 30 s on glow-discharged holey carbon grids (Quantifoil R2/2), onto which a home-made continuous carbon film ( $\sim$ 50 Å thick) had been deposited. Grids were blotted for 2.5 s in 100% ambient humidity and flash frozen in liquid ethane using an FEI Vitrobot. Grids were transferred to an FEI Titan Krios electron microscope operated at 300 kV. Images were collected using FEI's automated single particle acquisition software (EPU) and recorded on a back-thinned FEI Falcon II detector at a calibrated magnification of 104,478 (yielding a pixel size of 1.34 Å). An in-house system (37) was used to intercept the videos from the detector at a rate of 17 frames for each 1 s exposure. Defocus values ranged from 1.5-3.5  $\mu$ m. All datasets were collected under identical conditions.

### *Initial image processing*

Contrast transfer function parameters were estimated using CTFFIND3 (38). Particles were picked using semi-automated particle picking with RELION (39). All 2D and 3D classifications and refinements were performed using RELION (39). We used reference-free 2D class averaging to discard bad particles, leaving a total of 884,122 particles. 3D classification of all particles was used to isolate mitoribosome subpopulations, with each class subsequently refined. 3D refinements were initiated with a 60 Å low-pass filtered cryo-EM reconstruction of the yeast mitoribosome. Beam-induced particle movements were corrected using statistical movie processing in RELION (37, 40).

### *Masked refinement*

To improve the quality of the maps for both the mt-SSU and mt-LSU we firstly initiated independent refinement of each of the four collected datasets. The first dataset represents a reprocessing of the data used in (2). The resolutions for each dataset were 3.7, 4.0, 4.4 and 4.6 Å. The best two datasets (3.7 and 4.0 Å) were combined (286,106 particles) and the resultant 3D reconstruction analyzed for angular distribution. As some orientations had more particles assigned than others (as a result of preferential orientation of the mitoribosome on the EM grid), we selected alternative orientations from the 2D classifications for the other two datasets to improve the angular sampling. Combinations of these particles with the best two datasets gave a total of 449,823 particles. These data were 3D refined with soft masks applied (1) over the mt-LSU and mt-SSU and the head domain of the mt-SSU. For the mt-SSU, the resolution of the final reconstruction containing these additional particles (3.49 Å) was at a higher resolution than excluding the data (3.57 Å) or including all particles from all datasets (3.54 Å). The nominal resolution for the mt-LSU was 3.3 Å and for the masked head of the mt-SSU, 3.9 Å.

Prior to visualization, all density maps were corrected for the modulation transfer function (MTF), and then sharpened by applying a B-factor (Table S1) that was estimated using automated procedures (41).

### *Model building*

The revised Cambridge Reference Sequence (rCRS) (42) is used to number the mtDNA-encoded nucleic acid components of the mitoribosome. Ribosomal proteins are named following the new nomenclature (43) and rRNA helices are numbered corresponding to those in *Escherichia coli* (44).

The better resolved density for the mt-LSU allowed a number of improvements to our previously published model (2). For some regions, the structure of the porcine mitoribosome was used to guide model building (3). Improvements included the identification of mL54 (Uniprot ID: Q6P161) at the L7/L12 stalk and the extension of the termini of mL62 (ICT1) and the N-terminus of mL42. A number of additional features were also present at the subunit interface; the N-terminus of bL19m that faces the mt-SSU, a loop of bL19m (residues 198-212), the tip of rRNA H67 which forms bridge B7a, and a region of uL2m (residues 170-175) that contributes to mitochondria-specific bridge mB2. The density for the central protuberance was also much better resolved; this allowed identification of bL31m (Uniprot ID: Q7Z7F7) and rebuilding and extension of mL40, mL46 and mL48. Additional magnesium ions were also identified (Table S1). Additionally, the density for the nascent polypeptide in the exit tunnel is improved.

### *Refinement*

For optimal fitting of the model into the EM density map, we used REFMAC v5.8 adapted for EM refinement (1) to refine each subunit model against its masked map. To optimize stereochemistry at the subunit interface, the intact mitoribosome was refined against a composite map generated by combining the three masked maps (mt-LSU, mt-SSU and for the mt-SSU head). Intrasubunit external restraints were generated with ProSMART (45) using the models of the mt-SSU and mt-LSU that had been refined against the highest-resolution data. Restraints were not generated for the subunit interface to encourage conformational independence. To analyze the different conformation states of the human mitoribosome, the subunits were independently fit into the maps for each state using Chimera (46), and large-scale conformational changes within each subunit were manually adjusted using rigid-body fitting in Coot (47).

$FSC_{\text{average}}$  was monitored using during refinement to follow the fit-to-density, and the final model was validated using MolProbity (48). Cross-validation against over-fitting was calculated as previously described (1, 49) and refinement statistics are given in table S1.

### *Figures*

All figures were generated using PyMOL (50), Chimera (46) or QuteMol (51). Local resolution representations were created with ResMap (52). The secondary structure diagram of the mt-SSU rRNA was modified from the Comparative RNA website (53) using base pairs information extracted from the model using DSSR (54).

**Table S1.** Refinement and model statistics for the individual subunits and intact 55S mitoribosome. The mitoribosome was refined against a composite map formed from masked maps for mt-LSU, mt-SSU and the head domain of the mt-SSU.

<b>Data Collection</b>			
Particles	449,823		
Pixel size (Å)	1.34		
Defocus range (μm)	1.5 – 3.5		
Voltage (kV)	300		
Electron dose (e <sup>-</sup> Å <sup>-2</sup> )	25		
	<b>mt-SSU</b>	<b>mt-LSU</b>	<b>55S</b>
<b>Model composition</b>			
Non-hydrogen atoms	61,734	96,499	158,233
Protein residues	5,215	7,844	13,059
RNA bases	922	1,530	2,452
Ligands (Zn <sup>2+</sup> /Mg <sup>2+</sup> )	3/30	3/98	6/128
<b>Refinement</b>			
Resolution (Å)	3.49	3.27	3.30
Map sharpening B-factor (Å <sup>2</sup> )	-86	-106	various
Average B factor (Å <sup>2</sup> )	112	127	141
FSC <sub>average</sub>	0.88	0.86	0.85
<b>Rms deviations</b>			
Bonds (Å)	0.0076	0.0075	0.0064
Angles (°)	1.42	1.47	1.22
<b>Validation (proteins)</b>			
Molprobity score	2.8 (93 <sup>rd</sup> percentile)	2.6 (96 <sup>th</sup> percentile)	2.5 (98 <sup>th</sup> percentile)
Clashscore, all atoms	5.8 (100 <sup>th</sup> percentile)	5.2 (100 <sup>th</sup> percentile)	4.2 (100 <sup>th</sup> percentile)
Good rotamers (%)	86.6	89.8	91.2
<b>Ramachandran plot</b>			
Favored (%)	87.4	88.1	89.4
Outliers (%)	3.3	3.1	2.4
<b>Validation (RNA)</b>			
Correct sugar puckers (%)	97.1	95.9	97.2
Good backbone conformations (%)	68.0	65.3	66.5

**Table S2.** Mitochondrial ribosomal proteins (MRPs) of the human mt-SSU. Protein residues and signal peptide positions are numbered according to UniProt (55) with updated signal peptide cleavage positions based on the structure. Mitochondria-specific proteins were compared to known structures in the PDB using PDBeFold (56) and DALI (57).

MRP	Alias	UniProt ID	Chain ID	Mature protein (range, amino acids)	MW (excl. signal peptide, kDa)	Built residues (range, amino acids)	Notes
bS1m	MRPS28	Q9Y2Q9	W	72 – 187	13.1	77-173	OB motif. Structural homolog of the N-terminal domain of bS1.
uS2m	MRPS2	Q9Y399	B	1 – 296	33.2	58-274	
uS3m	MRPS24	Q96EL2	C	36 – 167	15.3	36-167	
uS5m	MRPS5	P82675	D	1 – 430	48.0	88-107; 126-150; 154-430	
bS6m	MRPS6	P82932	E	2 – 125	14.1	2-123	
uS7m	MRPS7	Q9Y2R9	F	38 – 242	24.1	35-53; 61-242	
uS9m	MRPS9	P82933	G	1 – 396	45.8	71-176; 198-396	
uS10m	MRPS10	P82664	H	1 – 201	23.0	61-182	
uS11m	MRPS11	P82912	I	1 – 194	20.6	59-194	
uS12m	MRPS12	O15235	J	30 – 138	12.1	31-138	
uS14m	MRPS14	O60783	K	1 – 128	15.1	28-128	
uS15m	MRPS15	P82914	L	58 – 257	23.5	66-229	
bS16m	MRPS16	Q9Y3D3	M	35 – 137	11.5	10-125	Zn-binding
uS17m	MRPS17	Q9Y2R5	N	21 – 130	12.3	5-111	
bS18b (mS40)	MRPS18-2	Q9Y676	O	1 – 258	29.4	52-236	Zn-binding
bS18c (bS18m)	MRPS18-1	Q9Y3D5	P	1 – 142	15.8	47-142	Zn-binding
bS21m	MRPS21	P82921	Q	1 – 87	10.7	2-87	
mS22	MRPS22	P82650	R	1 – 360	41.2	67-308	
mS23	MRPS23	Q9Y3D9	S	1 – 190	21.8	2-127	

mS25	MRPS25	P82663	T	1 – 173	20.1	2-163	Thioredoxin-like fold.
mS26	MRPS26	Q9BYN8	U	28 – 205	21.3	27-199	
mS27	MRPS27	Q92552	V	1 – 414	47.6	36-269; 278-291; 312-345; 355-400	Pentatricopeptide repeat proteins
mS29	MRPS29	P51398	X	19 – 398	43.4	51-168; 177-195; 220-398	Structurally similar to P-loop NTPases. GDP bound.
mS31	MRPS31	Q92665	Y	66 – 395	38.1	276-383	
mS33	MRPS33	Q9Y291	Z	2 – 106	12.5	5-91	
mS34	MRPS34	P82930	0	2 – 218	25.5	6-154; 162-213	
mS35	MRPS35	P82673	1	1 – 323	36.8	52-270; 287-323	Three domains; the NT domain contacts mS39. The middle domain has structural similarity to peptidyl-tRNA hydrolases including ICT1, and YaeJ and forms a shared $\beta$ -sheet with uS10. The C-terminal domain binds mS29.
mS37	MRPS37 (CHCHD1)	Q96BP2	2	1 – 118	13.5	2-117	
mS38	MRPS38 (AURKAIP1)	Q9NWT8	3	1 – 199	22.4	128-196	
mS39	MRPS39 (PTCD3)	Q96EY7	4	38 – 689	74.4	56-133, helices	Pentatricopeptide repeat protein.

**Table S3.** Comparison of mt-SSU rotations based on common superposition of the mt-LSU. PDB ID: 2J00 was used as the unrotated form (9) and PDB ID: 4JUW as the ratcheted form (10) of the bacterial ribosome. The screw axes and degree of rotation (°) were calculated with ProSMART (58).

	Bacterial ribosome		Human mitoribosome		
	Unrotated	Rotated	Class 1	Class 2	Class 3
<b>Unrotated</b>		8.0	7.4	9.0	14.4
<b>Rotated</b>	8.0		9.7	0.8	10.5
<b>Class 1</b>	7.4	9.7		9.2	9.5
<b>Class 2</b>	9.0	0.8	9.2		8.8
<b>Class 3</b>	14.4	10.5	9.5	8.8	

**Table S4.** Residues involved in intersubunit bridges. The analysis is based on class 1 with the exception of bridge mB7, which is specific to class 2. An analysis of bridge re-arrangement between the three classes is given in Table S5.

Bridge	Interaction type	mt-SSU component	Residues	mt-LSU component	Residues	Notes
B2a	RNA:RNA	rRNA h44	1490-1493; 1559-1562; 1582	rRNA H69	2576; 2581-2583	
B2b	RNA:RNA	rRNA h24	1071-1073	rRNA H67	2547-2548; 2590-2592	
B2c	RNA:RNA	rRNA h20	1058-1061	rRNA H66; rRNA H67	2511-2514; 2541-2543	
B3	RNA:RNA	rRNA h44	1502-1504; 1548-1550	rRNA H71	2610-2613; 2621-2624	
B5	Protein:RNA	rRNA h14	811-812	uL14m	43; 118; 120	
B7a	RNA:RNA	rRNA h23	1000-1001	rRNA H68	2558-2559	
B7b	Protein:RNA	rRNA h24	1062-1063	uL2m	231	
mB1a	Protein:protein	mS29	231-234	mL46	98-120 (partially modeled loop)	Unbuilt residues 168-177 from mS29 may also contribute.
mB1b	Protein:protein Protein:RNA	mS29 rRNA h42 rRNA h42	276-279; 1395-1396; 1412-1414	mL48 mL40	138-147 (unmodeled) C-terminal helix (194-201)	
mB2	Protein:protein	bS6m	24; 84-86	uL2m	171-174	
mB3	Protein:RNA	rRNA h27	1153-1154	rRNA H67	2543-2544	
mB4	Protein:RNA	mS38	151-152; 155-156; 159; 163	rRNA H71 rRNA H67	2595-2597; 2622-2623 2638-2640;	
mB5	RNA:RNA	rRNA h44	1505; 1539	uL14m	50-52	
mB6	Protein:protein	mS27	51; 87; 90; 93; 131; 134-135	bL19m	N-terminus	Poorly resolved; highly flexible
mB7	Protein:RNA	rRNA h23	981-982	uL2m	218	Specific to class 2.

**Table S5.** Bridge rearrangements for each subpopulation relative to class 1.

Bridge	Class 2	Class 3
B2a	Preserved.	Preserved.
B2b	Contact broken. rRNA h24 (bases 1072-1074) has moved by 6Å.	Contact broken. rRNA h24 (1072-1074) has moved by 5Å.
B2c	Contact broken. Bases 1059-1061 have shifted by 6-7Å. Possible new Mg-coordinated bridge between 1057-1058 and 2543-2544.	Contact broken. Bases 1059-1061 have shifted by 6-7Å.
B3	Unchanged.	Unchanged.
B5	A ~7Å shift of h14 results in closer contacts between the rRNA and uL14m.	~3Å shift of h14 results in closer contacts between the rRNA and uL14m.
B7a	Contact broken. 9Å shift of h23.	Contact broken. 8Å shift of h23.
B7b	Contact broken. Almost 8Å shift of h24.	Contact broken. 8Å shift of h24.
mB1a	Bridge has opened and nature of contacts changed.	Preserved despite movement of mS29.
mB1b	mS29 no longer contributes to the bridge due to a 17Å movement.	Preserved.
mB2	Widened by 3Å.	Broken. 12Å movement of bS6m.
mB3	Preserved.	Bridge opened by almost 4 Å.
mB4	Preserved.	Preserved.
mB5	Preserved.	Preserved.
mB6	Movement of mS27 towards bL19m.	Density is unclear.
mB7	Bridge specific to class 2.	Absent.



**Table S6.** Mutations in MRPs of the mt-SSU.

MRP	Mutation	Clinical significance	References	Possible Effect
bS16m	R111X	Corpus callosum agenesis, hypothonia and fatal neonatal lactic acidosis	(59)	Nonsense mutation results in premature degradation of bS16m.
mS22	R170H	Edema, cardiomyopathy, tubulopathy, and hypotonia	(60)	Mutation R170H in mS22 might sterically disturb the interprotein $\beta$ -sheet arrangement that forms binding site of mS22 onto bS16m.
mS22	L215P	Cornelia de Lange-like syndrome oedema, cardiomyopathy and tubulopathy	(61)	Mutation results in premature degradation of mS22. mS22 helps stabilize uS5m at the mRNA channel entrance.

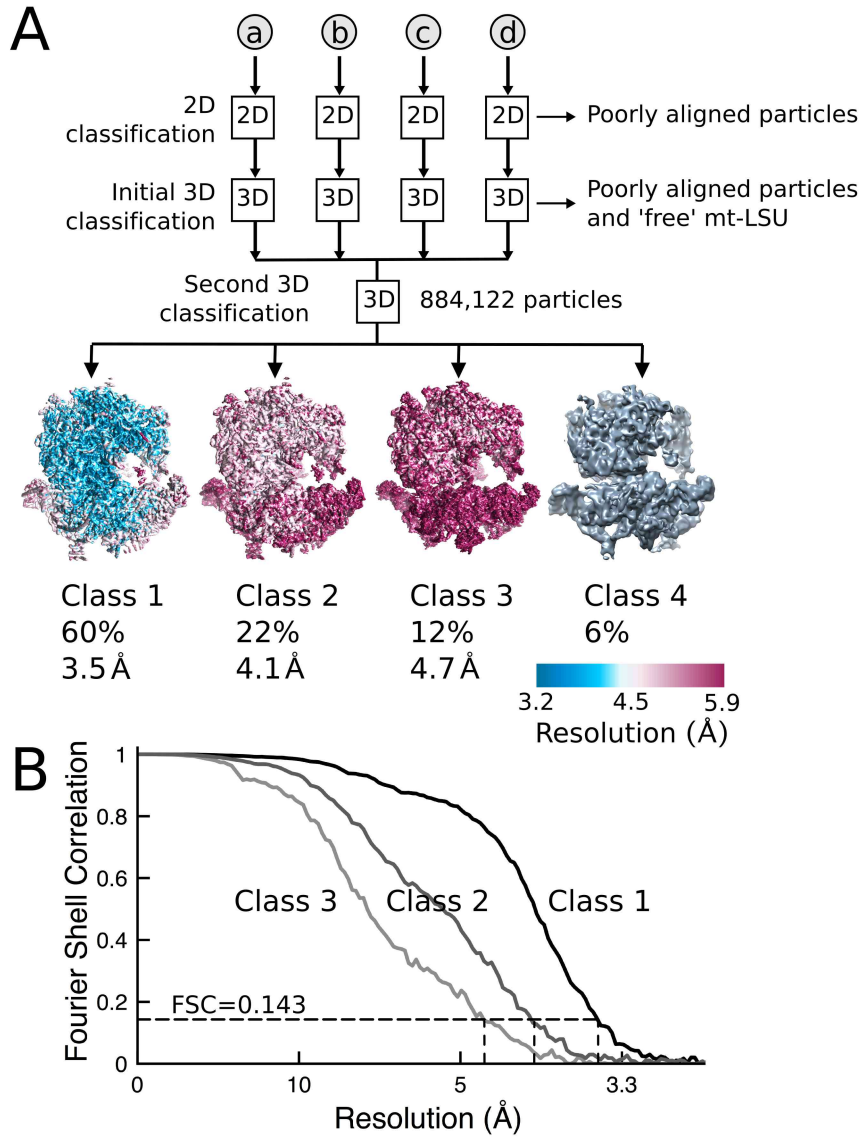


**Fig. S1.** *In silico* processing of mitoribosome datasets. **A.** After initial removal of poorly aligned particles and 'free' mt-LSU by 2D and 3D classification, a subsequent round of 3D classification with the retained particles from all datasets reveals three distinct conformations of the human mitoribosome (classes 1-3, sorted by population size) that are colored by local resolution. Class 4 represents particles that aligned poorly. **B.** 'Gold-standard' FSC plots for the three classes.

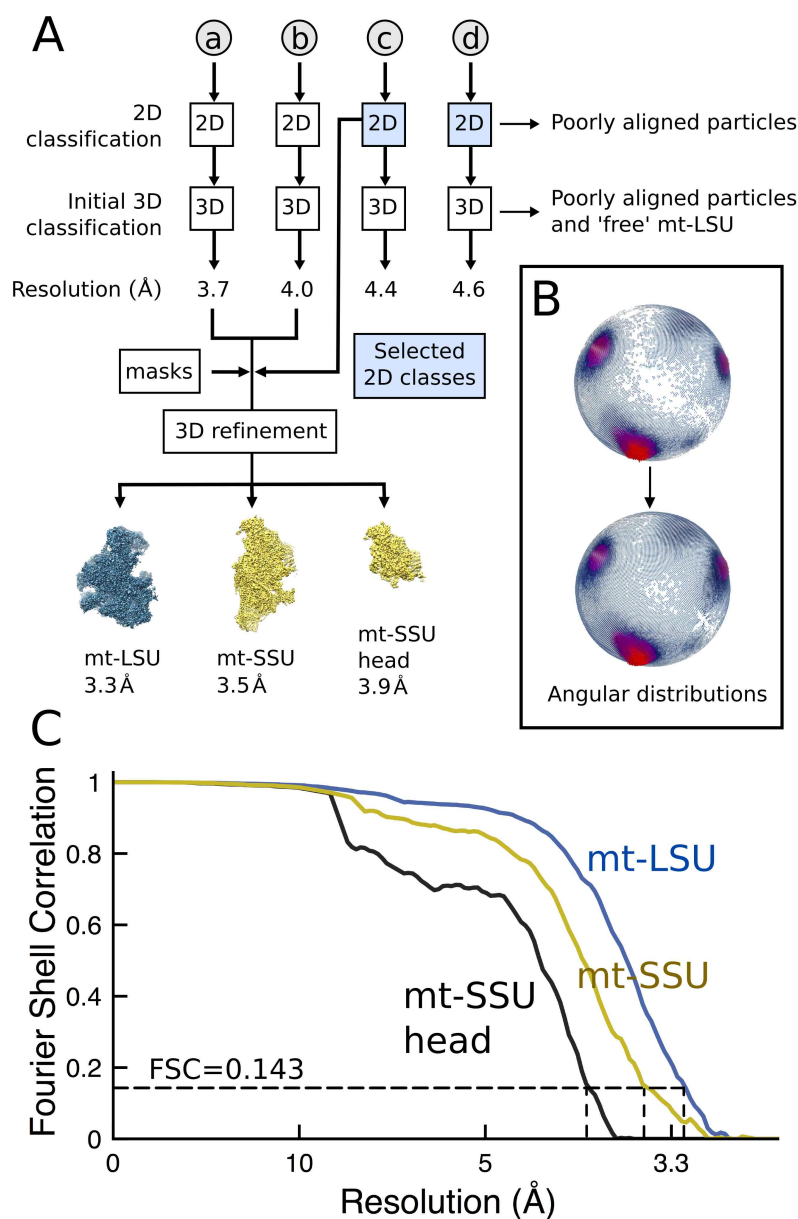


**Fig. S2.** To improve the resolution of the maps for model building we utilized map refinement using masked maps. Each dataset was initially processed separately as described in (2). This resulted in four maps that reached nominal resolutions of 3.7, 4.0, 4.4 and 4.6 Å. The two datasets at highest resolution were combined and supplemented with views extracted from 2D-classification of the remaining datasets (c and d) that were poorly represented in the first two datasets. 3D refinement of these data with masks applied over the mt-LSU, mt-SSU and head region improved the resolution of these maps to 3.3, 3.5 and 3.9 Å, respectively. Local resolutions for these masked maps are given in Fig. 1. **B.** Projection of the first two euler angles on a sphere in an arbitrary orientation. Each point of the sphere represents a different projection direction. The length of the cylinder represents how many individual particles are assigned to that direction. There is a linear scale for both the height of the cylinder from low to high number of particles and from blue to red. The angular distribution improves when datasets a and b (top) are supplemented with additional 2D classes from datasets c and d (bottom). **C.** FSC curves for the masked maps.

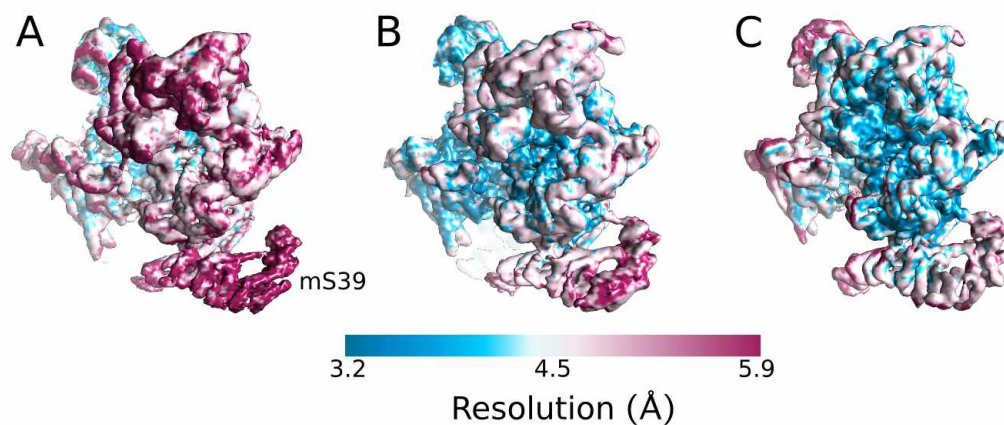


**Fig. S3.** The local resolution of the mt-SSU head is improved by applying masks during refinement (see Fig. 1). **A.** View of the head region of the mt-SSU of the intact mitoribosome (class 1) without masking reveals that the head is poorly resolved due to conformational variability. **B.** Masking of the mt-SSU improves the local resolution to approximately 4-5 Å. **C.** Subsequent masking of only the head domain improves the local resolution further to aid model building of this region, particularly for mS39.

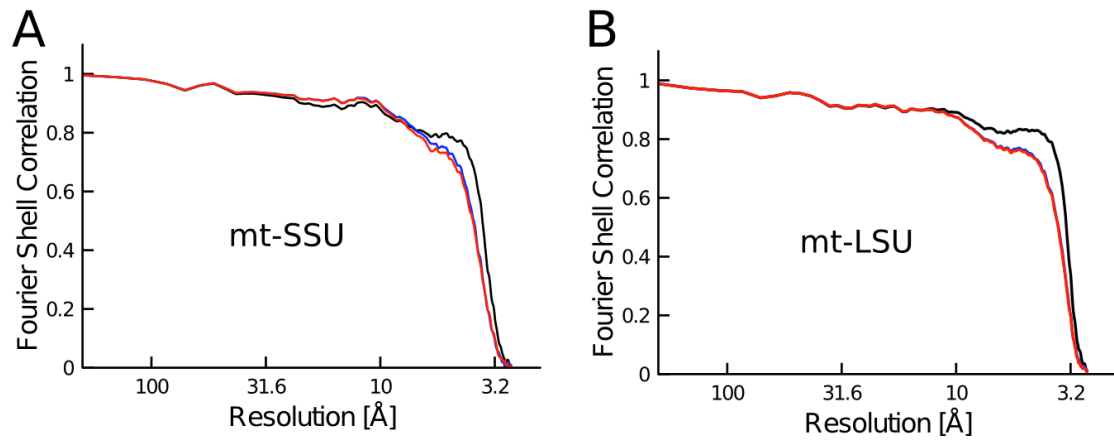


**Fig. S4.** Overfitting was monitored using cross-validation (1, 49). Fourier shell correlation curves were calculated between the refined model and the final map (black), along with the self (FSC<sub>work</sub>, blue) and cross-validated (FSC<sub>test</sub>, red) correlations. FSC curves for mt-LSU (A) and mt-SSU (B) demonstrate that no overfitting of the final models is apparent.

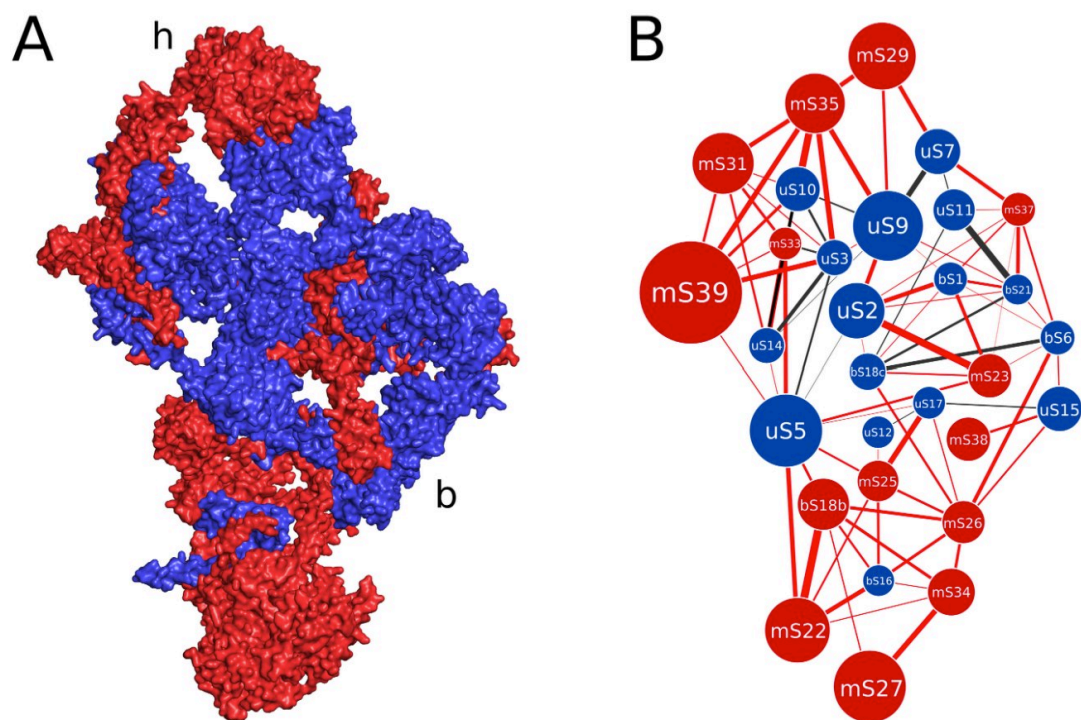


**Fig. S5.** Interactions between mitoribosomal proteins of the mt-SSU. **A.** Surface representation showing interaction between mitoribosomal proteins with homologs in bacteria (blue) and mitochondria-specific proteins (red). **B.** Protein-protein network of A. The node size represents the relative molecular mass of the protein and the edge thickness the solvent accessible surface buried in the interface. Interactions conserved with bacteria are shown in black, and mitochondria-specific interactions in red. The protein-protein network for the mt-LSU is given in ((*ref. 2*)).

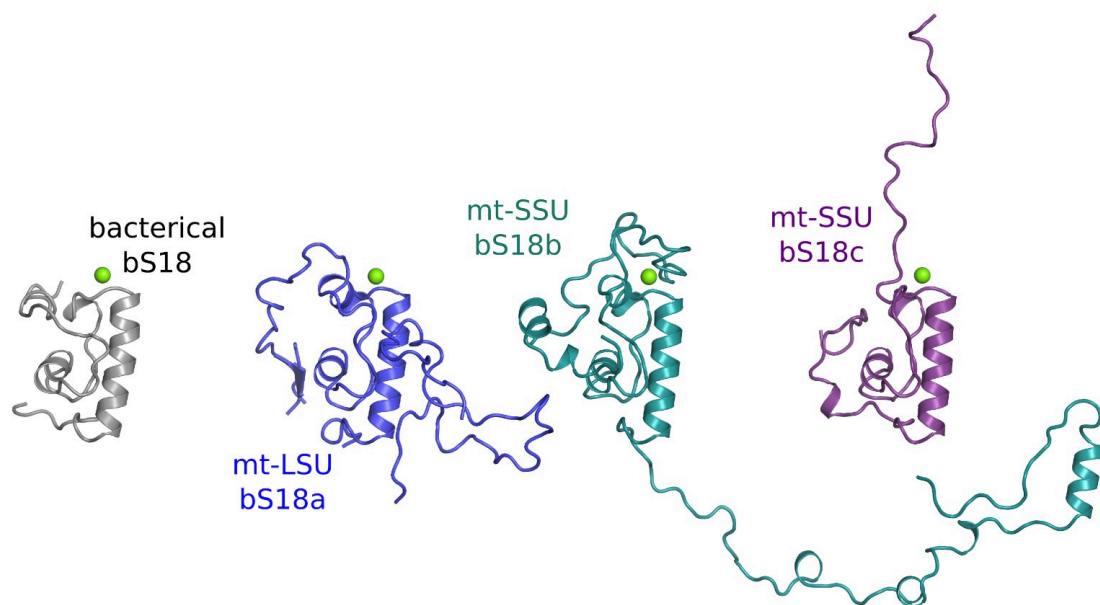


**Fig. S6.** The human mitoribosome contains three structural homologs of bS18; one in the mt-LSU and two in the mt-SSU. While the Zinc (green sphere) binding motif is conserved the N- and C-termini extensions do not show any conservation.



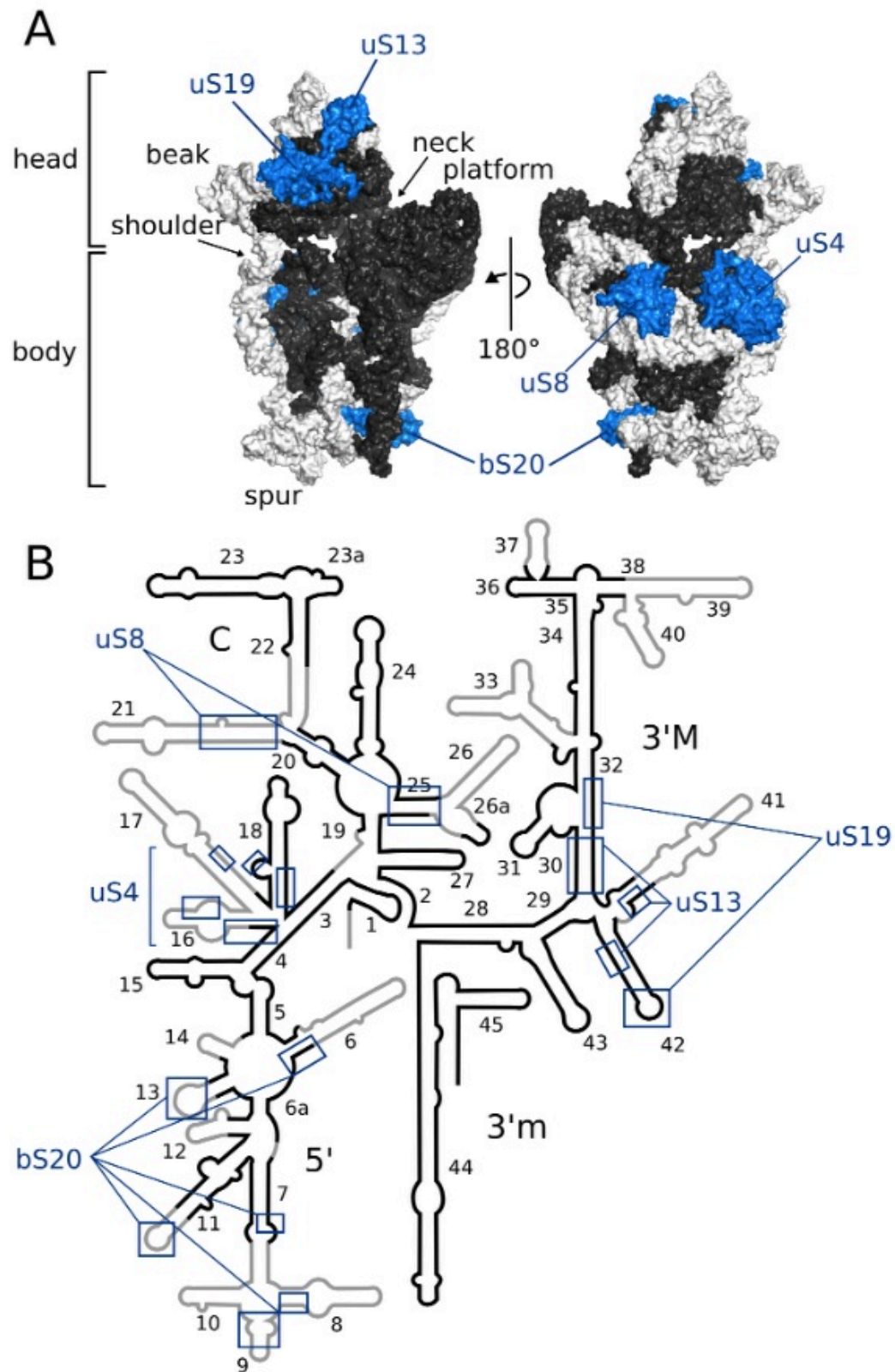


**Fig. S7. A.** Surface representation showing the contraction of mt-SSU rRNA. rRNA present in both bacteria and human mitoribosomes is shown in black, and excised sections in white. Proteins absent from the mitoribosome, but observed in bacteria are shown in blue. **B.** Secondary structure representation of A.



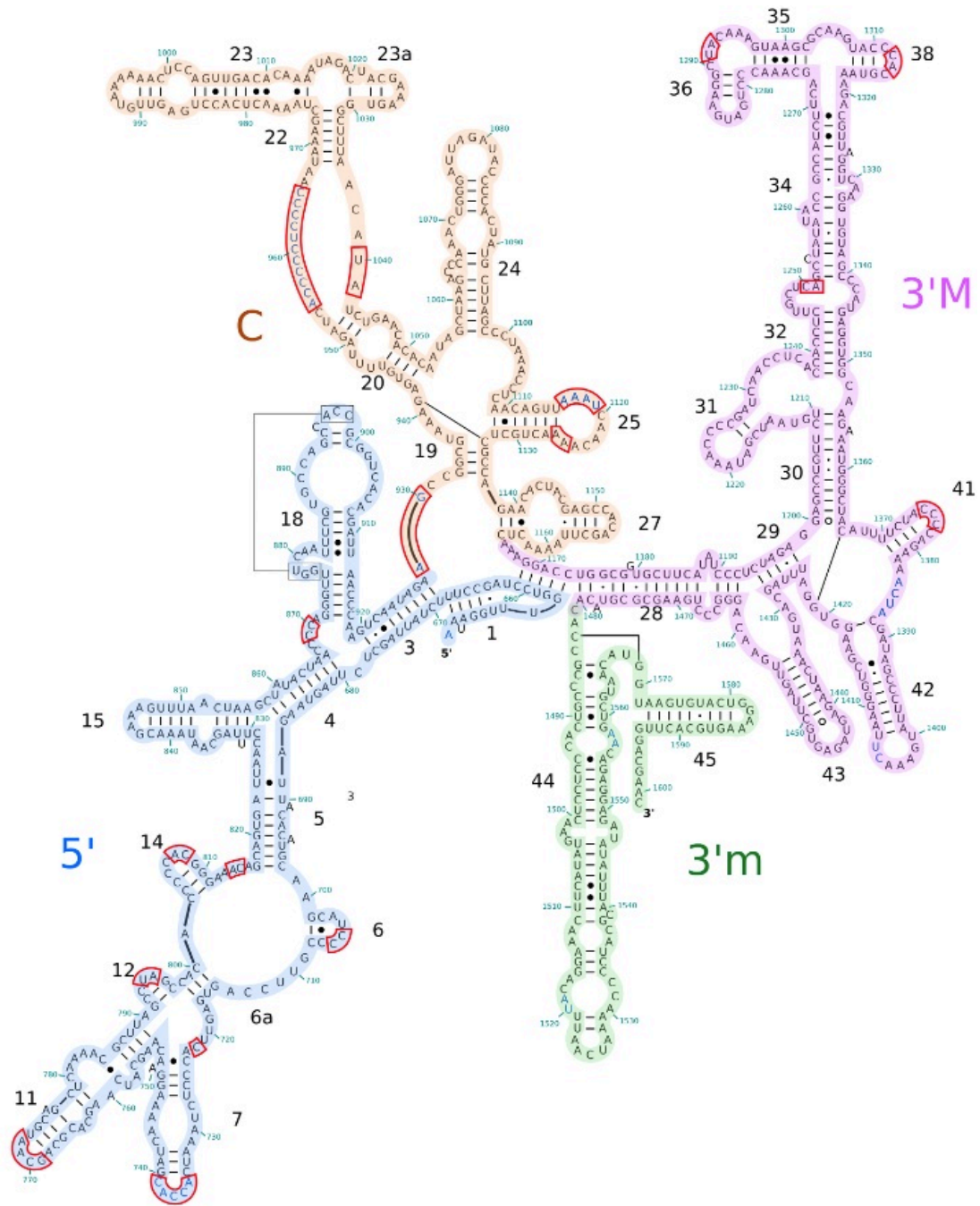


**Fig. S8.** Secondary structure diagram for mt-SSU rRNA colored by domain. Sections that bridge conserved regions are highlighted in red. Unbuilt regions are shown in blue lettering.

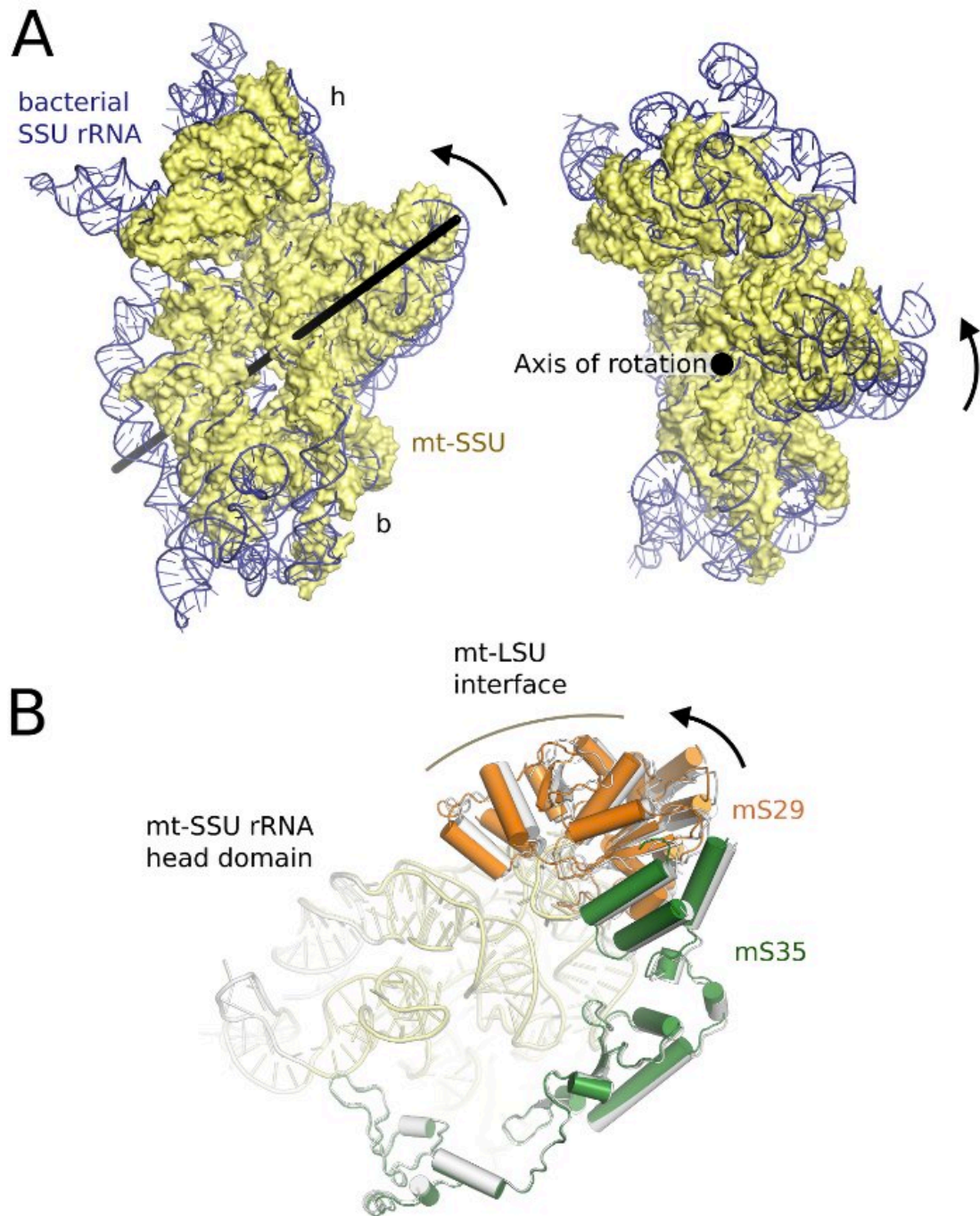


**Fig. S9. A.** Based on common superposition of the large subunits, mt-SSU is related to the bacterial SSU in the unrotated form (9) by a  $7.4^\circ$  rotation around an axis that runs through h44 and h3 (black line). **B.** Superposition of the mt-SSU from classes 1 and 2 reveals that the rRNA head domains align with very little movement. Independent of rRNA head movement, the mS29 and the C-terminal domain of mS35 move by  $3.4 \text{ \AA}$  that alters the contacts with central protuberance of the mt-LSU. Class 1 is shown in grey, and class 2 in color.

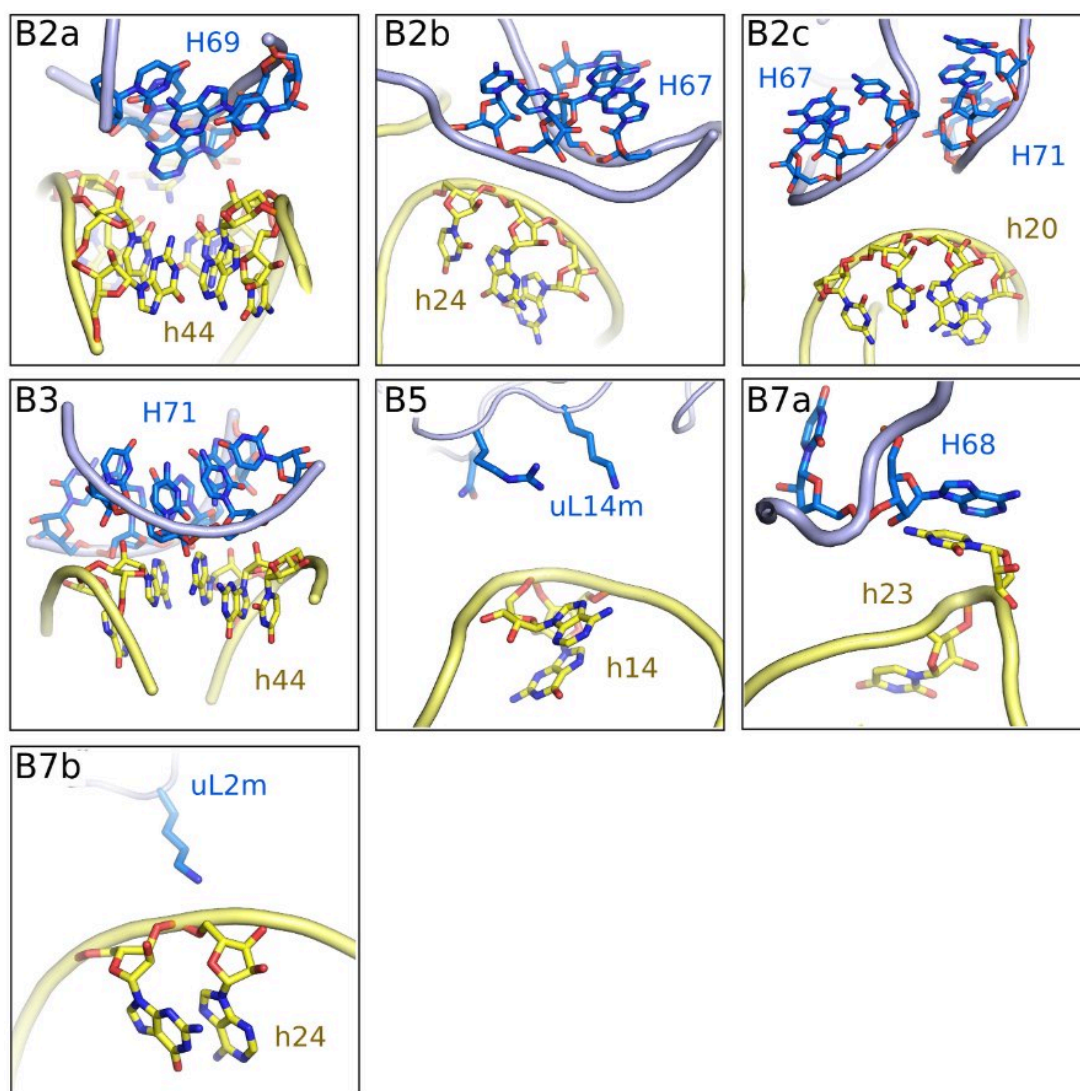


**Fig. S10.** Bridges conserved with bacterial and cytoplasmic ribosomes.

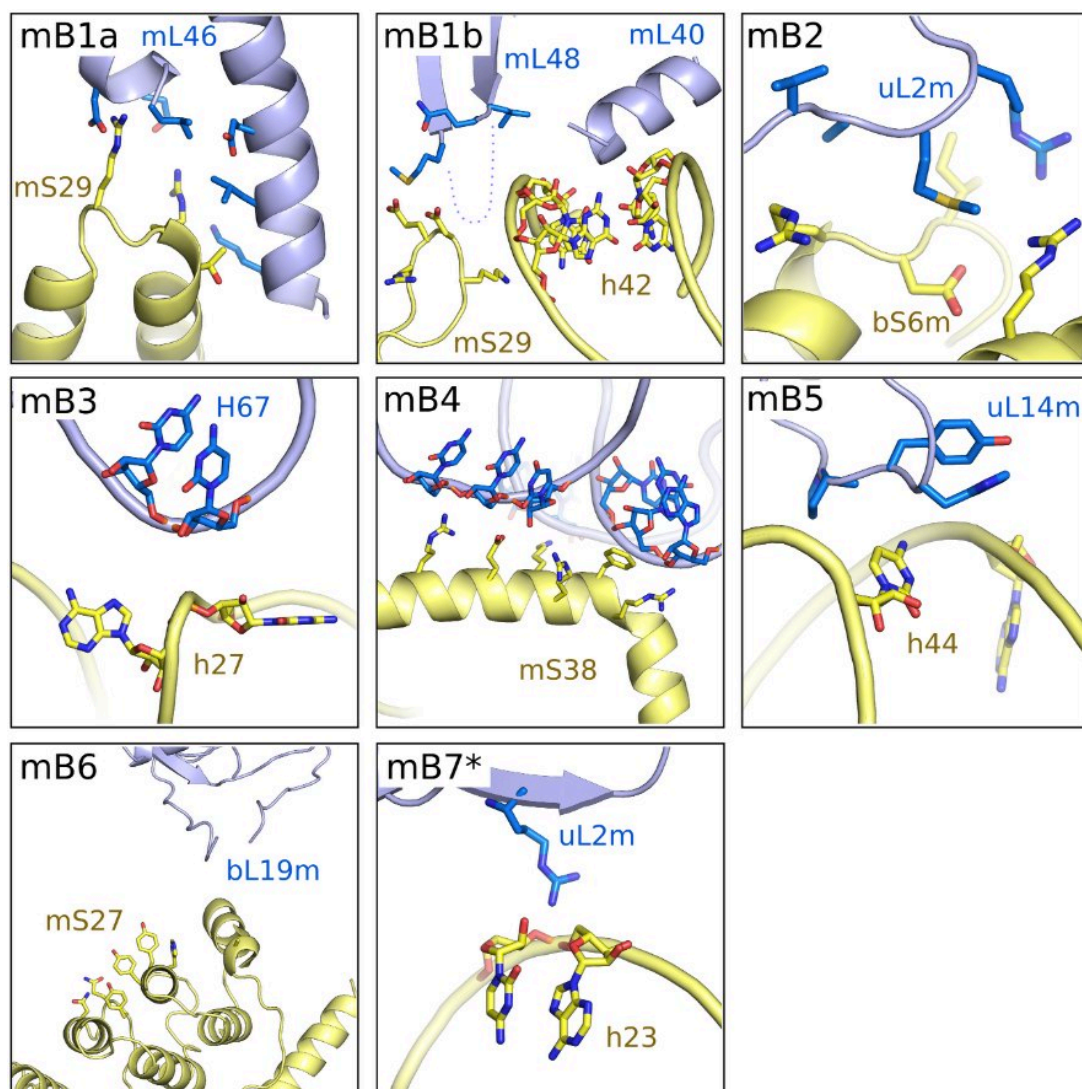


**Fig. S11.** Intersubunit bridges specific to mitoribosomes. mB7 is only observed in the ratcheted form (class 2).



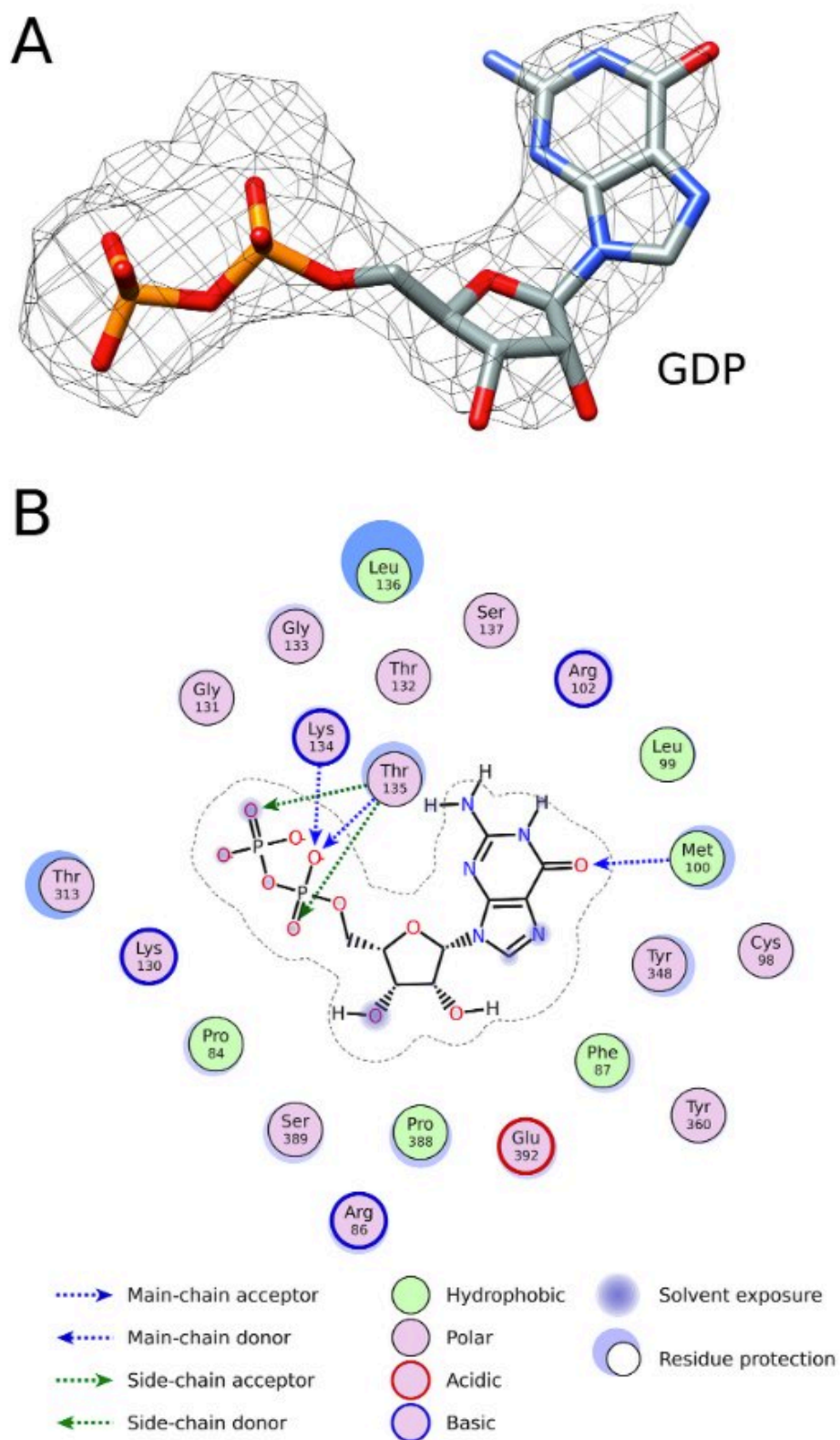


**Fig. S12.** **A.** mS29-bound GDP showing map density (mesh). **B.** Environment of the bound GDP. A hydrogen bond between the carbonyl group of the guanosine moiety and the main chain amide of Met100 contributes to the specificity for GDP over ADP.

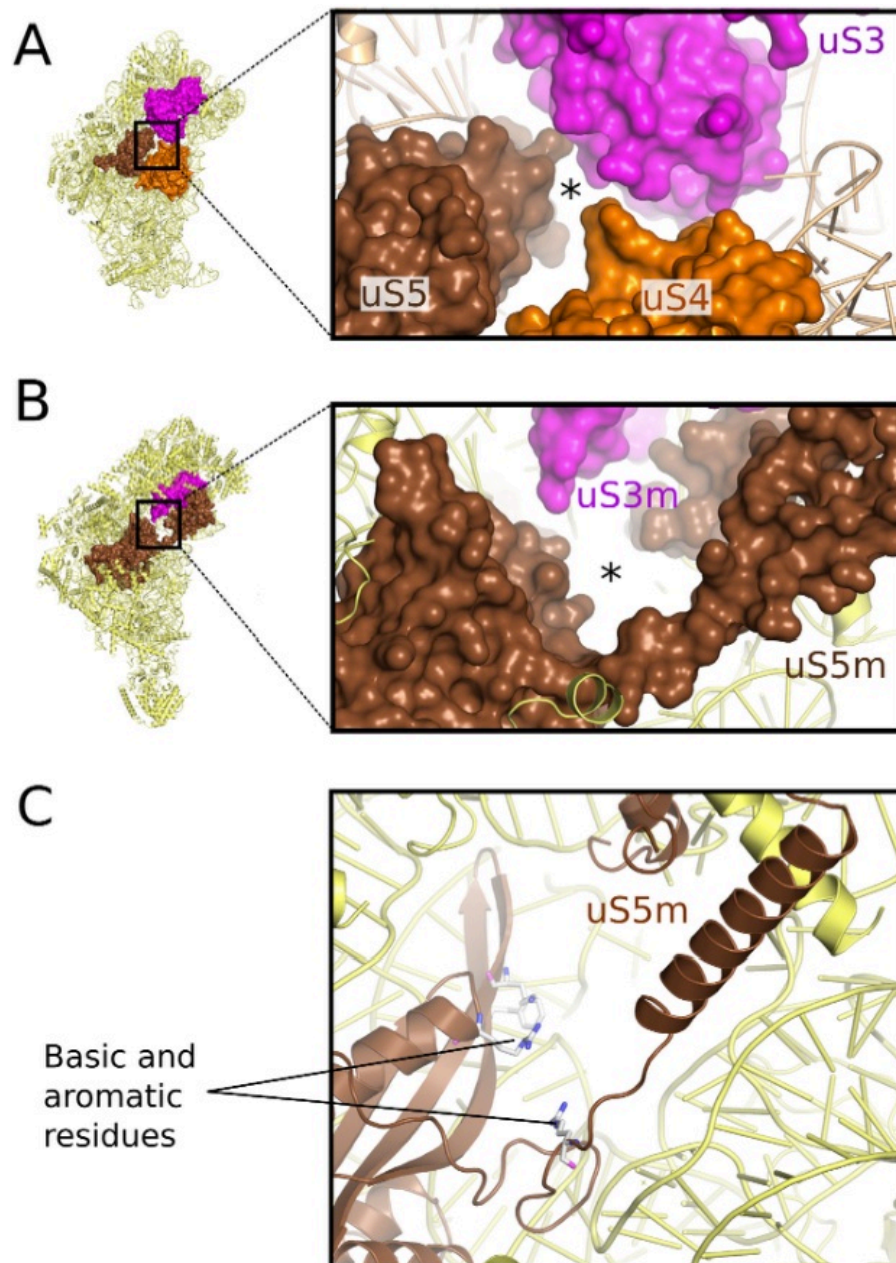


**Fig. S13.** **A.** The channel entrance in bacteria. uS3 and uS4 confer helicase-like activity on the ribosome. **B.** The channel entrance in the human mitoribosome is wider due to the absence of uS4 and the N-terminal domain of uS3. A mitochondria-specific extension of uS5m partially fills the void left by uS4. **C.** uS5m lays out the channel interior with basic (Arg189, Lys239, Arg264) and aromatic (Phe229) residues, which might be involved in direct interactions with mRNA.

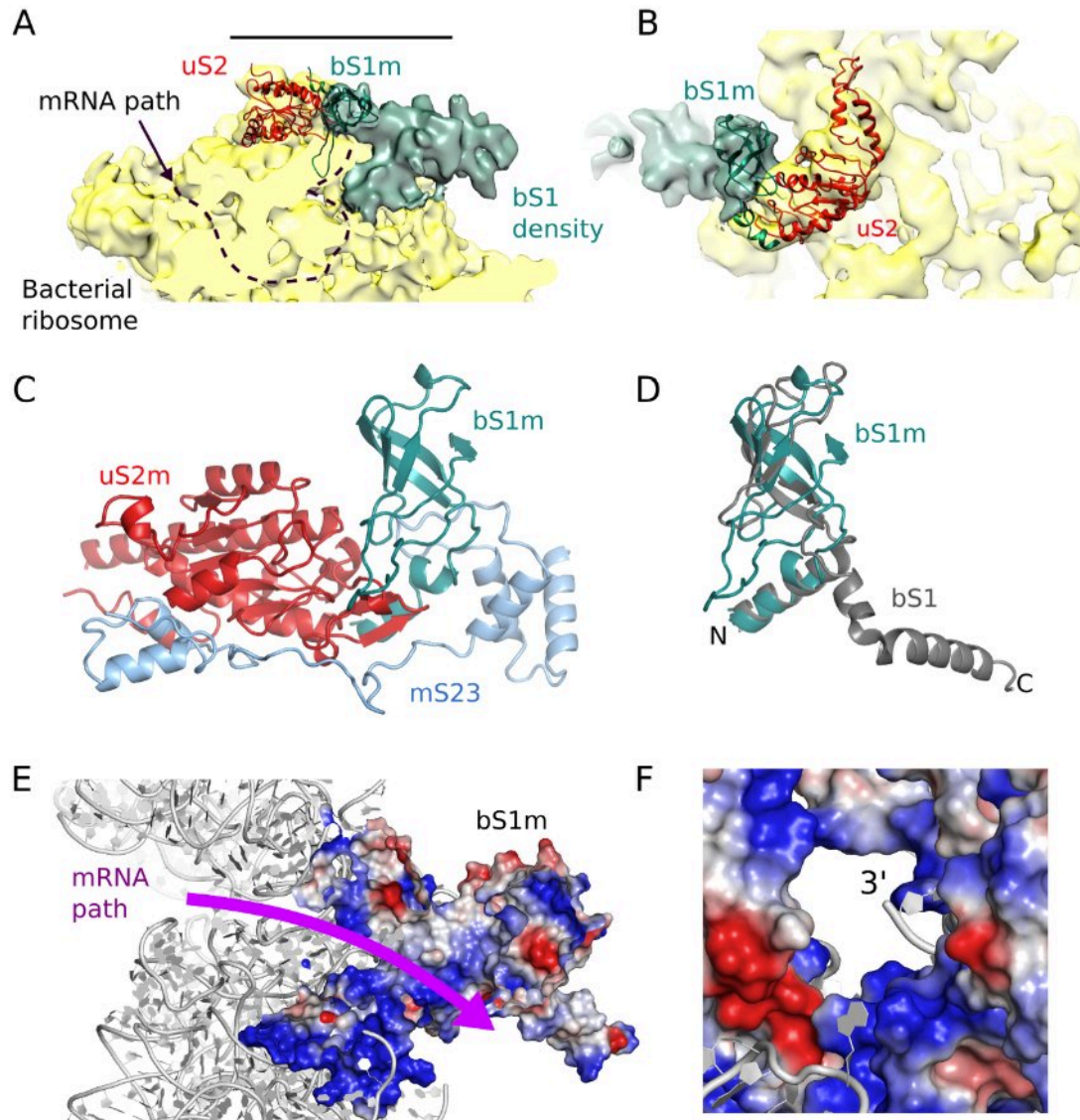


**Fig. S14.** **A.** The location of bS1m is compatible with a low-resolution map of bS1 bound to the bacterial ribosome (EMD-5693). **B.** A view from above as indicated in A. **C.** bS1m is tightly bound to the mitoribosome through extensive interactions with uS2m and mS23. **D.** Superposition of bS1m with the N-terminal domain of bS1 (PDB ID: 4Q7J). bS1m lacks the C-terminal helix that connects consecutive OB-folds in bS1. **E.** Surface representation of bS1m, bS21m and mS37 showing electrostatic potential. The surface of bS1m facing the channel and the channel exit (**F**) are electropositive.



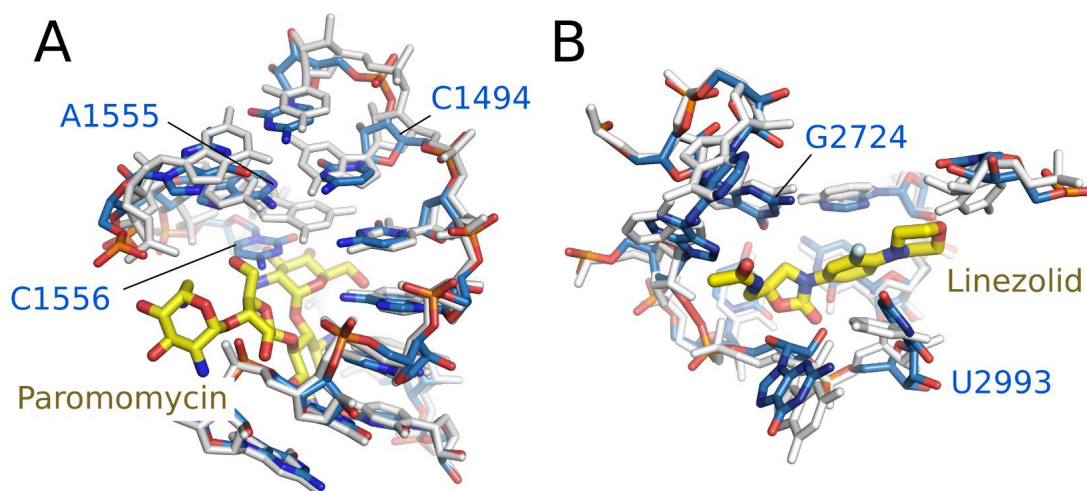


**Fig. S15. A.** Paromomycin is a member of the aminoglycoside class of antibiotics. It binds adjacent to the A site of the decoding center of the bacterial rRNA (grey) and induces codon-anticodon misreading and prevents translocation of mRNA:tRNA to the P site. The binding site in the human mt-rRNA (blue) is more flexible due to loss a G:C base pair. Mutations in three residues surrounding the binding site would induce a more bacteria-like conformation and are implicated in aminoglycoside hypersensitivity (Table S6). **B.** The binding pocket near the A site in the mt-LSU rRNA (blue) for oxazolidinones (including linezolid) is nearly identical to that observed in bacteria (shown in grey) (62, 63). In both panels, antibiotics are shown in yellow.



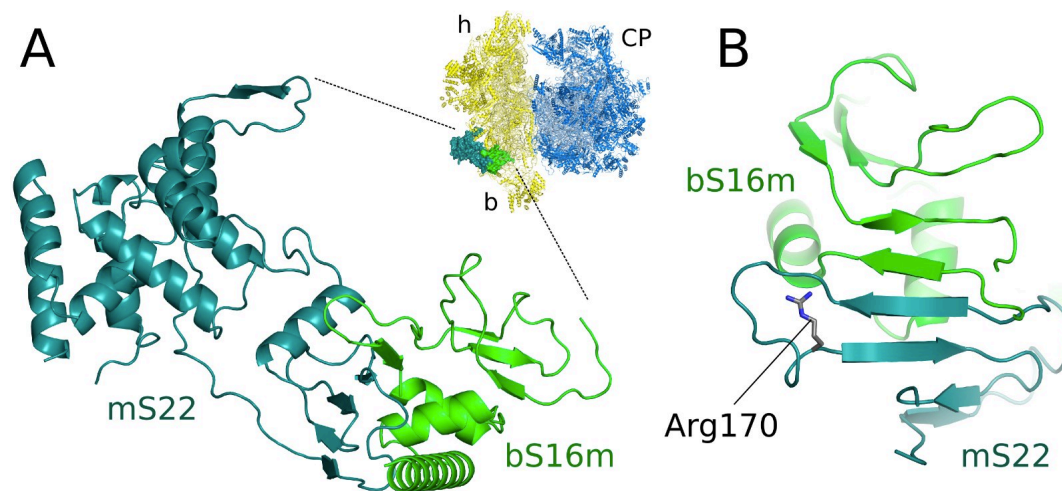


**Fig. S16.** Mutations in the mt-SSU proteins bS16m and mS22 are associated with pathological phenotypes (Table S3). **A.** bS16m and mS22 are located on the solvent side of the mt-SSU body and are tightly associated through a shared  $\beta$ -sheet. Both a nonsense mutation in bS16m (Arg111Stop) and a missense mutation in mS22 (Leu215Pro) result in premature degradation of the protein product (59, 61). Absence of either protein would result in a destabilization of the lower body, including uS5m that forms part of the mRNA channel entrance. **B.** Mutation Arg170His in mS22 might sterically hinder the formation of the interprotein  $\beta$ -sheet with bS16m.

## References

1. A. Amunts *et al.*, *Science* **343**, 1485 (2014).
2. A. Brown *et al.*, *Science* **346**, 718 (2014).
3. B. J. Greber *et al.*, *Nature* **515**, 283 (2014).
4. W. Zhang, J. A. Dunkle, J. H. Cate, *Science* **325**, 1014 (2009).
5. M. Heublein *et al.*, *Mol Biol Cell* **25**, 3342 (2014).
6. SOM,
7. Y. Chen, S. Feng, V. Kumar, R. Ero, Y. G. Gao, *Nat Struct Mol Biol* **20**, 1077 (2013).
8. M. S. VanLoock *et al.*, *J Mol Biol* **304**, 507 (2000).
9. M. Selmer, *Science* **313**, 1935 (2006).
10. D. S. Tourigny, I. S. Fernandez, A. C. Kelley, V. Ramakrishnan, *Science* **340**, 1235490 (2013).
11. J. A. Dunkle, L. Wang, M. B. Feldman, A. Pulk, V. B. Chen, *Science* **332**, 981 (2011).
12. T. V. Budkevich *et al.*, *Cell* **158**, 121 (2014).
13. S. Mohan, J. P. Donohue, H. F. Noller, *Proc Natl Acad Sci U S A* **111**, 13325 (2014).
14. M. R. Sharma *et al.*, *Cell* **115**, 97 (2003).
15. P. S. Kaushal *et al.*, *Proc Natl Acad Sci USA* **111**, 7284 (2014).
16. J. Chen, A. Tsai, S. E. O'Leary, A. Petrov, J. D. Puglisi, *Curr Opin Struct Biol* **22**, 804 (2012).
17. A. Ben-Shem *et al.*, *Science* **334**, 1524 (2011).
18. W. Wong *et al.*, *Elife* e03080 (2014).
19. N. D. Denslow, J. C. Anders, T. W. O'Brien, *J Biol Chem* **266**, 9586 (1991).
20. H. R. Kim *et al.*, *FASEB J* **21**, 188 (2007).
21. J. E. Walker, M. Saraste, M. J. Runswick, N. J. Gay, *EMBO J* **1**, 945 (1982).
22. G. Z. Yusupova, M. M. Yusupov, J. H. Cate, H. F. Noller, *Cell* **106**, 233 (2001).
23. S. Takyar, R. P. Hickerson, H. F. Noller, *Cell* **120**, 49 (2005).
24. S. M. Davies *et al.*, *FEBS Lett* **583**, 1853 (2009).
25. P. Yin *et al.*, *Nature* **504**, 168 (2013).
26. N. Manavski, V. Guyon, J. Meurer, U. Wienand, R. Brettschneider, *Plant Cell* **24**, 3087 (2012).
27. J. Montoya, D. Ojala, G. Attardi, *Nature* **290**, 465 (1981).
28. J. Rabl, M. Leibundgut, S. F. Ataide, A. Haag, N. Ban, *Science* **331**, 730 (2011).
29. K. Byrgazov, S. Manoharadas, A. C. Kaberdina, O. Vesper, I. Moll, *PLoS ONE* **7**, e32702 (2012).
30. X. Qu, L. Lancaster, H. F. Noller, C. Bustamante, I. J. Tinoco, *Proc Natl Acad Sci U S A* **109**, 14458 (2012).
31. D. Takeshita, S. Yamashita, K. Tomita, *Nucleic Acids Res* **42**, 10809 (2014).
32. J. A. Caminero, G. Sotgiu, A. Zumla, G. B. Migliori, *Lancet Infect Dis* **10**, 621 (2010).
33. K. M. Keeling, D. Wang, S. E. Conard, D. M. Bedwell, *Crit Rev Biochem Mol Biol* **47**, 444 (2012).
34. E. Selimoglu, *Curr Pharm Des* **13**, 119 (2007).
35. Y. Qian, M. X. Guan, *Antimicrob Agents Chemother* **53**, 4612 (2009).
36. A. Soriano, O. Miro, J. Mensa, *N Engl J Med* **353**, 2305 (2005).
37. X.-C. Bai, I. S. Fernandez, G. McMullan, S. H. Scheres, *eLife* **2**, e00461 (2013).
38. J. A. Mindell, N. Grigorieff, *J Struct Biol* **142**, 334 (2003).
39. S. H. W. Scheres, *Journal of Structural Biology* **180**, 519 (2012).

40. S. H. Scheres, *Elife* **3**, e03665 (2014).
41. P. B. Rosenthal, R. Henderson, *J Mol Biol* **333**, 721 (2003).
42. R. M. Andrews *et al.*, *Nature genetics* **23**, 147 (1999).
43. N. Ban *et al.*, *Current Opinion in Structural Biology* (2014).
44. P. Maly, R. Brimacombe, *Nucleic Acids Research* **11**, 7263 (1983).
45. R. A. Nicholls, F. Long, G. N. Murshudov, *Acta crystallographica. Section D, Biological crystallography* **68**, 404 (2012).
46. E. F. Pettersen *et al.*, *J Comput Chem* **25**, 1605 (2004).
47. P. Emsley, B. Lohkamp, W. G. Scott, K. Cowtan, *Acta crystallographica. Section D, Biological crystallography* **66**, 486 (2010).
48. V. B. Chen *et al.*, *Acta crystallographica. Section D, Biological crystallography* **66**, 12 (2009).
49. I. S. Fernandez, X.-C. Bai, G. Murshudov, S. H. W. Scheres, V. Ramakrishnan, *Cell* (2014).
50. W. L. DeLano, (2002).
51. M. Tarini, P. Cignoni, C. Montani, *IEEE Trans Vis Comput Graph* **12**, 1237 (2006).
52. A. Kucukelbir, F. J. Sigworth, H. D. Tagare, *Nature methods* **11**, 63 (2014).
53. J. J. Cannone *et al.*, *BMC bioinformatics* **3**, 2 (2002).
54. X.-J. Lu, W. K. Olson, *Nature protocols* **3**, 1213 (2008).
55. U. Consortium, *Nucleic Acids Research* **41**, D43 (2013).
56. E. Krissinel, K. Henrick, *Acta crystallographica. Section D, Biological crystallography* **60**, 2256 (2004).
57. L. Holm, P. Rosenström, *Nucleic Acids Research* **38**, W545 (2010).
58. R. A. Nicholls, M. Fischer, S. McNicholas, G. N. Murshudov, *Acta Crystallogr D Biol Crystallogr* **70**, 2487 (2014).
59. C. Miller *et al.*, *Ann Neurol* **56**, 734 (2004).
60. A. Saada *et al.*, *J Med Genet* **44**, 784 (2007).
61. P. Smits *et al.*, *Eur J Hum Genet* **19**, 394 (2011).
62. J. A. Ippolito *et al.*, *Journal of Medicinal Chemistry* **51**, 3353 (2008).
63. D. N. Wilson *et al.*, *Proceedings of the National Academy of Sciences* **105**, 13339 (2008).